Multiple time-scales of decision making in the hippocampus and prefrontal cortex

Authors: Wenbo Tang[1,3], Justin D. Shin[1,3] and Shantanu P. Jadhav[1,2,]*

Affiliations:

[1]Graduate Program in Neuroscience, Brandeis University, Waltham, MA, 02453, USA.

[2]Neuroscience Program, Department of Psychology, and Volen National Center for Complex Systems, Brandeis University, Waltham, MA, 02453, USA.

[3]These authors contributed equally to this work

*Correspondence to: shantanu@brandeis.edu

Abstract

Neural activity underlying decision making has been reported in many brain regions in the form of choice-specific neuronal sequences that span entire task periods. In contrast to this behavioral-timescale activity, recent work has raised the possibility of fast-timescale decision-making activity in hippocampal and prefrontal regions. Whether these are distinct or complementary mechanisms is unknown. Here, we examined simultaneous hippocampal and prefrontal ensemble activity during learning of a spatial working-memory decision task. We found that both regions formed choice-specific sequences at the behavioral timescale (~seconds), as well as two fast timescales (~100-200 ms), theta cycles during navigation and sharp-wave ripples in inter-trial periods. Behavioral-timescale sequences maintained representations of current goals during navigation. In contrast, at the fast timescales, hippocampal sequences supported deliberation, whereas prefrontal ensembles predicted actual choices. Error trials resulted from impaired interaction between behavioral- and fast-timescale mechanisms. These results establish cooperative interaction at multiple timescales for memory-guided decision making.

Introduction

The neural substrates that support decision making are still not fully understood. The link between decision making and neural representations at the behavioral timescale has been studied extensively in various cortical and sub-cortical circuits of different species. Early classic work showed that during tasks involving sustained attention or decision making, neurons in the prefrontal cortex (PFC) and the posterior parietal cortex (PPC) can exhibit persistent activity over seconds throughout retention intervals for maintenance of decision-related information[1-4]. In contrast to these low-dimensional representations that require long-lived stable states, decision-related information can also be held in a dynamic population code. At the ensemble level, heterogenous activity patterns comprising sequences of neuronal activation that span entire task periods have emerged as a common coding scheme in many brain regions, including PFC[5,6], hippocampus[6,7], PPC[8,9] and striatum[10,11].

In addition to this behavioral-timescale activity, recent work has raised the possibility that neural dynamics at fast, cognitive timescales that occur transiently during discrete subsets of task periods can also underlie upcoming decisions. In many brain areas, such as prefrontal, parietal, orbitofrontal cortices, and hippocampus, population activity can change in an abrupt, coordinated, and transient manner in support of flexible decisions[12-16]. For example, discrete transient bursts of gamma and beta oscillations in PFC have been shown to increase with working-memory load during delays[14]. In particular, recent studies have identified time-compressed neuronal sequences in the hippocampus and also PFC as a specific cell-assembly pattern at fast timescales that can support decision-making processes. Hippocampal theta sequences provide time-compressed ensemble representations of spatial paths within single cycles of theta oscillations (6-12 Hz) during active navigation, which reflect a candidate neural mechanism for planning at decision time[16-19],

although whether these sequences exist in PFC has yet to be determined. Conversely, during pauses in exploration, replay sequences are observed both in the hippocampus and PFC during individual sharp-wave ripples (SWRs)[20-22], reactivating past and future trajectories on the temporal scale of 100-200 ms to guide navigation decisions[20]. Disruption of these fast sequences in the hippocampus, while leaving behavioral-timescale spatial representations intact, impairs navigation decisions[23-26]. Thus, fast sequences are promising transient activity patterns that could support decision making at sub-second speed[17,18,20,27]. Whether and how these fast-timescale representations are linked to behavioral-timescale mechanisms for decision making is unknown, with the possibility that they represent either distinct or co-operative decision making modes. To address these questions, we examined neuronal ensemble activity simultaneously in the hippocampus and PFC of rats during learning of a spatial working-memory decision task.

Results

Slow and fast sequences during navigation decisions

We trained nine rats to learn a spatial working-memory task (**Fig. 1a**), which has been previously reported to require both the hippocampus and PFC[23,24,28,29], and involves memory-guided decision making[20,23,30]. In this continuous alternation W-track task, animals had to remember their past choice between two possible locations (the left or L vs. right or R arm; inbound reference memory task), and then choose the opposite arm correctly when facing the two upcoming options after running through a delay section on the center stem (outbound working memory task; **Fig. 1b**). All subjects learned the task rules over eight training sessions in a single day (**Supplementary Fig. 1**; final performance: 92.5 ± 1.8% for inbound, 80.8 ± 2.8% for outbound, in mean ± SEM).

Using continuous recordings over learning in the experimental paradigm, we examined the ensemble activity of dorsal CA1 hippocampal and PFC neurons at different timescales (**Fig. 1c,d** and **Supplementary Fig. 1**; mean ± SEM = 43.9 ± 7.6 CA1 place cells, 29.8 ± 5.6 PFC cells per session). We first verified the presence of CA1 place-cell sequences at both the slow behavioral timescale (i.e., place-field sequences) and the fast compressed timescales (i.e., theta sequences during navigation, and replay sequences at reward wells; **Fig. 1d**). Interestingly, PFC cell assemblies appeared to be organized into sequences at these timescales as well, and could occur concurrently with the hippocampal sequences (**Fig. 1d**). Given these observations, we further investigated the content of these sequences and their roles in decision making.

Slow behavioral-timescale sequences predict behavioral choices

First, we characterized how slow behavioral-timescale sequences encode animals' location and choice. Consistent with prior reports[5,6,20,31,32], we found that many CA1 and PFC cells exhibited strong preferential firing during navigation on L- versus R- side trajectory (trajectory-selective cells; mean ± SEM = 38.4 ± 1.2% in CA1, 23.5 ± 1.3% in PFC for inbound, 35.0 ± 0.7% in CA1, 20.9 ± 0.6% in PFC for outbound; **Fig. 2a,b** and **Supplementary Fig. 2**). These trajectory-selective cells, when ordered by the peak firing on the preferred trajectory, form a unique sequence for each choice type spanning the entire trial length, including the common center stem prior to the choice point (CP) and the side arms after the CP (**Fig. 2c,d**). Different sequences of neurons were thus activated on L vs. R trials at the behavioral timescale (**Fig. 2c,d**). To directly assess the cell-assembly representation of the animals' choices, we used a memoryless Bayesian decoding algorithm (see **Methods**)[20]. We found that cell assemblies in CA1 and PFC consistently predicted the animals' current location and choice at the behavioral timescale well above chance level across

all positions of a trial[5,6,20,31], even on the common center stem (**Fig. 2e,f** and **Supplementary Fig. 2**), and this decoding accuracy increased with familiarity with the task (**Fig. 2e,f** and **Supplementary Fig. 2**) as in previous reports[20].

Therefore, these results suggest that choice information progresses through heterogeneous neuronal sequences in CA1 and PFC at the behavioral timescale as rats run along each trajectory. Importantly, the unique representations of different trial types at the behavioral timescale also provide distinguishable templates for the Bayesian decoder to determine the content of fast sequences during theta oscillations and SWRs.

Look-ahead fast theta sequences in CA1 and PFC

Theta oscillations are prominent in CA1 during navigation, and prior work has found that CA1 cell assemblies are organized into theta sequences within single oscillation cycles that encode paths ahead of the animal, potentially providing a "look-ahead" prediction of upcoming locations[33,34]. While it is not known whether PFC activity is directly related to hippocampal theta sequences, previous studies have shown that PFC cells phase-lock to hippocampal theta oscillations[35,36]; further, theta-frequency synchrony and coherent spatial coding between the hippocampus and PFC is apparent during memory-guided navigation[37-39]. To detect theta sequences, population spikes within each candidate hippocampal theta cycle ($\geq$ 5 cells active in a given brain region) during active running were analyzed using the Bayesian decoding approach, and the sequential structure of the Bayesian reconstructed positions was evaluated by shuffling procedures (see **Methods**). Using this method, clear theta sequences were found in CA1 during inbound and outbound navigation across all sessions (**Fig. 3a-f**), and the majority of CA1 theta sequences (~70%) successively represented past, present, and future locations within each theta cycle (forward

6

sequences; **Supplementary Fig. 3**), consistent with previous studies[33,40]. Intriguingly, significant theta sequences were also detected in PFC (**Fig. 3g-l**), and the prevalence of theta sequences in PFC was similar to that in CA1 (**Supplementary Fig. 3a**), although higher trajectory scores (suggesting more reliable timing of sequences) were observed in CA1 compared to PFC (**Supplementary Fig. 3b**). Furthermore, the trajectory scores and slopes (sequence speed) in both regions increased with experience (**Supplementary Fig. 3b,c**).

Notably, for forward-shifted theta-sequence representations, when reconstructed positions in different theta-phase bins were averaged over all candidate theta cycles, we found that the positions behind the actual location of the animal were decoded with higher probability during inbound than outbound navigation in both CA1 and PFC (**Fig. 4a,b**). To further confirm this result, we directly compared the start and end positions of each significant theta sequence, and indeed, forward sequences in both CA1 and PFC started farther behind the actual position of the animal during inbound than outbound navigation (**Fig. 4c**). Previous theoretical and experimental evidence has suggested that the initial tail of asymmetric spatial fields allows cells with fields ahead of an animal's position to fire during earlier theta cycles, which results in "look-ahead" of theta sequences[33,34,41]. We therefore examined whether there was any relationship between firing field asymmetry and the shift in ahead-sequence length during outbound and inbound navigation (**Fig. 4d-g**). Quantification of field asymmetry revealed that while the asymmetry developed with experience as reported previously (**Fig. 4d-f**)[41], working-memory-guided outbound navigation was associated with fields with a more extended initial tail compared to inbound travel (**Fig. 4d-f**), and this was stronger for trajectory-selective than non-selective cells in both CA1 and PFC (**Fig. 4g**). Additionally, CA1 and PFC cells had similar slopes of theta phase precession for inbound and

outbound navigation (**Supplementary Fig. 4**), which thus cannot explain the difference in inbound and outbound look-ahead of theta sequences.

Together, these results suggest that beyond the pure sensory features of the environment, memory demands influenced the look-ahead properties of theta sequences in both CA1 and PFC, and the increased look-ahead distance during working-memory-guided outbound navigation allows the animal to represent future locations earlier in the trajectory, which can aid in decision making.

Theta sequences support vicarious memory recall

How do theta sequences relate to the animals' upcoming choices, and do they represent these choices throughout navigation similar to the behavioral-timescale sequences? To test this, we examined theta sequences along each trajectory (**Fig. 5**). We found distinct representations of choices by theta sequences in CA1 and PFC, which were dependent on task phases (i.e. prior to and after the decision or choice point, CP). Before the CP (corresponding to periods on the center stem for outbound navigation), CA1 theta sequences serially encoded both alternative trajectories (**Fig. 5a,e** and **Supplementary Fig. 5**), in agreement with prior work that observed hippocampal theta activity patterns representing hypothetical scenarios, which can support deliberation[16,18]. However, after the choice was made, CA1 theta sequences preferentially encoded the animal's current choice (**Fig. 5b,e** and **Supplementary Fig. 5**). In contrast, PFC theta sequences preferentially encoded the animal's current choice throughout a trial (**Fig. 5c-e** and **Supplementary Fig. 5**). This effect was robust across sessions (**Fig. 5e**), enabling trial-by-trial prediction of decisions, in which upcoming choice was decoded by PFC theta sequences well above chance before the CP, whereas CA1 theta sequences encoded actual and alternative

8

available paths equivalently before the CP (**Fig. 5f,g**). Similar results were found for inbound trials (**Supplementary Fig. 5**). Note that these results could not be accounted for by similar spatial-field templates for L versus R choices on the center stem, because spatial-field activity can decode L versus R choices well above chance within the center stem in both CA1 and PFC, and this decoding accuracy was higher for CA1 than PFC (**Fig. 2e,f**). We also controlled for the last theta sequence on the center stem and found similar effects (**Supplementary Fig. 5l**). A previous study has reported that alternating representations of possible future choices in the hippocampus are linked to single-cell cycle skipping, in which cells fire on alternate theta cycles[18]. Here, we confirmed the expression of cycle skipping in CA1, and we found that PFC cells clearly exhibited this phenomenon as well (**Supplementary Fig. 6**).

Next, we asked if PFC theta sequences encoded choices that were coherent with CA1 sequences within single theta cycles. We detected PFC theta sequences simultaneously with CA1 theta sequences for a subset of theta cycles (**Fig. 5h,i**; mean $\pm$ SEM $= 10.53 \pm 1.42\%$ for outbound, $11.17 \pm 1.52\%$ for inbound; $p = 0.78$ comparing outbound vs. inbound proportions, rank-sum test). Among these synchronous sequence events, when CA1 theta sequences represented the actual choice, PFC sequences were also significantly biased to the actual choice, whereas this coherent CA1-PFC representation was not observed when CA1 theta sequences represented the alternative choice (**Fig. 5j**).

Taken together, these results suggest that CA1-PFC theta sequences occurred in tandem with, but distinct from, behavioral-timescale sequences for choice representations, and that CA1-PFC theta sequences underlie a novel mechanism that supports vicarious memory recall on a fast timescale for deliberative decision making.

Fast replay sequences prime decisions

While we found a clear relationship between CA1 and PFC sequences at both behavioral and theta timescales for upcoming decisions, it remains unclear if these contributed to correct versus erroneous decisions. We therefore analyzed neural activity during correct versus incorrect trials, with incorrect trials corresponding to erroneous outbound navigation to the same side arm as the past inbound visit (**Fig. 6a**). We found that sequential firing that occurred at the behavioral timescale during incorrect trials was similar to that during correct trials (**Fig. 6b**), and the decoding accuracy for the chosen side was comparable for correct and incorrect trials (**Fig. 6c**). Furthermore, CA1 and PFC theta sequence prediction of upcoming choice was also similar for correct and incorrect trials (**Fig. 6d**). Correct versus incorrect trials did not differ in running speed and theta power (**Supplementary Fig. 7a,b**). CA1-PFC theta coherence and the strength of single-cell phase-locking to theta oscillations during navigation, which have been proposed to support spatial working memory[37], were also similar between correct versus incorrect trials (**Supplementary Figs. 7c,d** and **8**). Therefore, both theta-linked phenomena at the two timescales likely represented maintenance mechanisms for working memory and decision making, making it plausible that incorrect destinations were chosen prior to embarking on trajectories from the center well.

We therefore examined replay sequences during SWRs in the inter-trial periods prior to trajectory onset (**Fig. 1c,d**). Previously, we have reported that CA1 replay sequences, similar to its theta sequences, underlie deliberation between actual and alternative choices, whereas CA1-PFC reactivation represents actual choice for current trials[20]. Here, we confirmed these observations (**Fig. 7a** and **Supplementary Fig. 9**). Importantly, using CA1-PFC reactivation strength for actual versus alternative choices preceding the correct and incorrect trials, we could predict correct and incorrect responses significantly better than chance (**Fig. 7b** and **Supplementary Fig. 9c**),

indicating impaired CA1-PFC reactivation prior to incorrect outbound navigation. Furthermore, quantification of SWR reactivation using a standard cell-pair measure revealed that incorrect decisions were distinctively associated with impaired reactivation of the trajectory-selective CA1-PFC cell pairs (**Fig. 7c,d** and **Supplementary Fig. 9d,e**). These results suggest that CA1-PFC replay sequences during awake SWRs prime initial navigation decisions, which are further maintained by theta-sequence and trajectory-selective mechanisms during retention periods on a trial-by-trial basis, underlying successful performance in the working memory task.

Discussion

Our findings provide a new framework that integrates behavioral-timescale and cognitive-timescale mechanisms for memory-guided decision making. The presence of prominent sequential activation patterns of hippocampal-prefrontal ensembles at multiple timescales during spatial working memory tasks offers a unique opportunity to dissect the neural mechanisms at different timescales for decision making. By studying hippocampal-prefrontal population coding at multiple timescales, we demonstrate that two forms of cell-assembly dynamics for decision making can be distinguished, i.e., slow behavioral-timescale sequences and fast cognitive-timescale sequences. During delay periods of the spatial navigation task, choice information was maintained by behavioral-timescale sequences in CA1 and PFC on correct as well as incorrect trials. These sequences are contextually modulated by current journeys and goals, and can enable choice-related information processing on a behavioral timescale for planning actions[6,9]. In contrast, compressed-timescale sequences during theta oscillations and sharp-wave ripples were strongly modulated by internal cognitive states beyond current external context, retaining representations of actual and alternative options. Such representations can support continuous internal exploration of

11

possibilities, suggesting a novel role of compressed sequences in guiding ongoing choice behavior. This is in contrast to models of deliberative decision making via accumulation of evidence to a threshold[42]. Notably, the mechanism of using internally generated sequences to simulate future scenarios has been used as a key feature that improves performance of model-based learning computations[19,43,44].

At the level of single theta cycles, we found compressed theta sequences in both CA1 and PFC nested within the behavioral-timescale sequences during navigation. However, these two types of theta-associated sequences are functionally dissociated. We found that prior to the decision-making point in the navigation task, CA1 theta sequences report both actual and alternative choices, and are unable to predict chosen destination till after the decision has been made. On the other hand, we found robust PFC theta sequences that maintain prediction of upcoming choice prior to the decision point. Thus, theta sequences underlie a cognitive timescale mechanism that also maintains choice information, with the key distinction that this fast timescale mechanism can support vicarious memory recall of different choices, which was not seen at the behavioral timescale. This process may be important in the event that animals have to change decisions or adapt to change in contingencies[15,27,30]. In agreement with this idea, a recent study has shown that theta timescale mechanisms in CA1 can not only represent possible future paths, but also possible directions of motion on a moment-to-moment basis[18]. Representation of past locations within theta cycles has also been recently reported[45]. Complementing these results, previous studies have shown that theta oscillation cycles comprise cognitive computation units, corresponding to segregation of cell assemblies that represent different spatial experiences[46-48] and alternatives[16-18]. The results shown here establish that the representation of alternatives in the

hippocampus interacts with prefrontal theta sequences in a content-specific manner, which can be used to guide actual choices.

Notably, both theta-associated mechanisms during navigation supported retention during working memory periods, but did not predict errors in decisions. Rather, we found that compressed SWR replay sequences during inter-trial periods prior to the onset of trajectories prime the decision without apparent external cue triggers, which is maintained from the onset of the trajectory via behavioral and theta timescale sequences. Previous studies have shown that SWR-reactivation in the hippocampus is less coordinated prior to incorrect versus correct trials[20,49], and disrupting awake SWRs leads to increase in errors in the spatial working memory task[23,24]. Consistent with these results, our findings provide definitive evidence that coherent CA1-PFC replay of future trajectories indicate the chosen destination in this memory-guided decision making task, and errors in CA1-PFC replay predict incorrect decisions.

It is important to note that the expression of behavioral- and compressed-timescale sequences representing different trajectories are inextricably linked. Choice-specific representations of both theta and replay sequences depend on choice encoding through trajectory preferred firing of behavioral-timescale sequences. Furthermore, incorrect decisions were specifically associated with replay of the trajectory-selective neurons in PFC and CA1, with trajectory selectivity inherently a behavioral-timescale characteristic. Thus, it is the interactions between behavioral-timescale and fast cognitive-timescale firing properties that govern decision making. The network mechanisms that enable expression of sequences at distinct timescales in multiple circuits remain a key question for future investigation.

Overall, our results provide a critical extension to classic models, which emphasize behavioral-timescale activity patterns typically spanning entire retention intervals, by establishing

a role of discrete, fast timescale ensemble activity patterns in decision making processes. Such a mechanism is broadly supported by recent findings of rapid shifts in activity patterns during decision making[12,13,15,50], including discrete gamma oscillatory bursts in PFC underlying working memory[4,14], which occur at a similar timescale to compressed theta and replay sequences. Together, these results suggest the possibility of transient LFP oscillations as informative signatures of fast evolving cell assemblies that bear on decision-making processes, and the cooperative behavioral- and cognitive-timescale mechanisms described here may reflect a general organizing principle of neural dynamics underlying decision making.
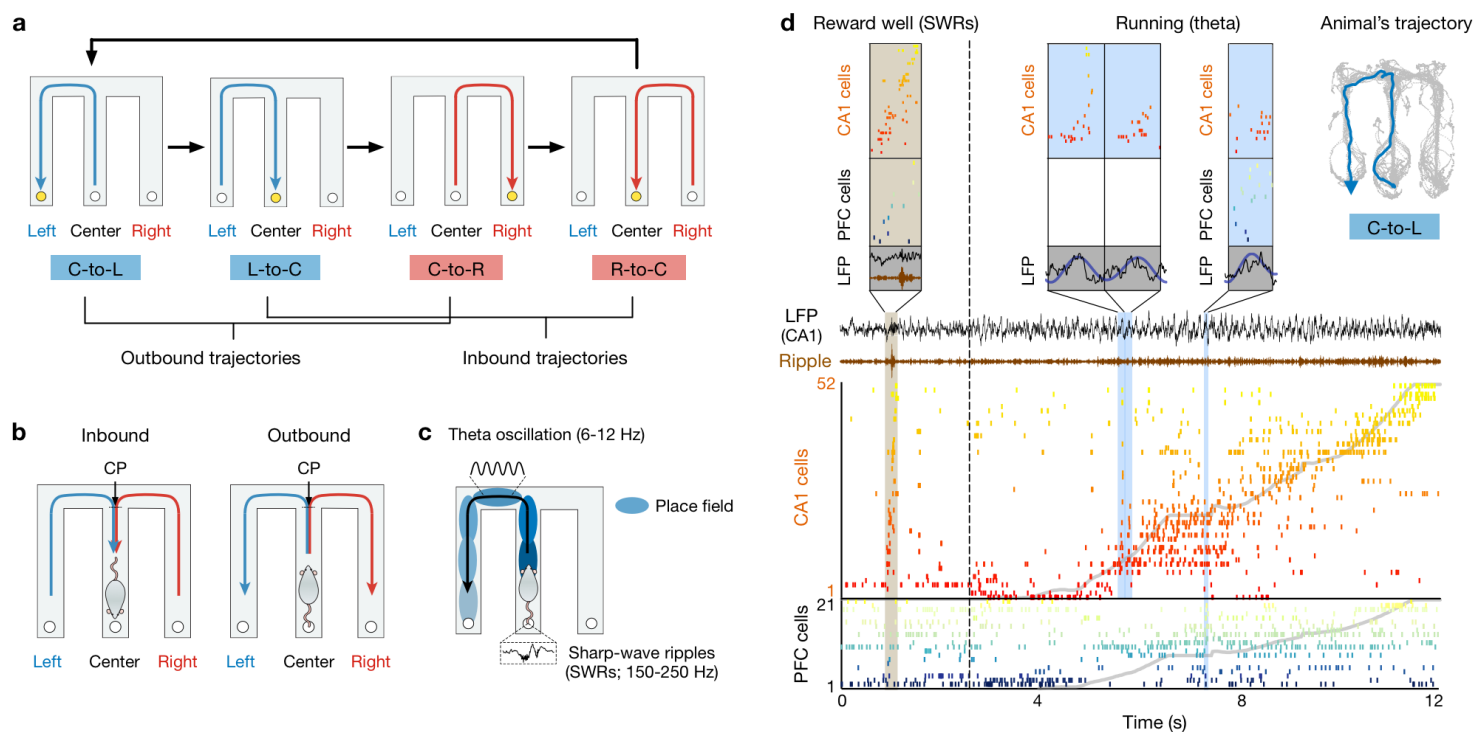
Main Figures and Legends

Fig. 1| Sequential organization of CA1 and PFC cell assemblies at multiple timescales during navigation decisions. a, W-maze spatial alternation task. In this task, rats are rewarded (yellow circle) for choosing between Left (L) versus Right (R) in the correct order shown. **b,** Diagrams of two possible past (inbound; *left*) and future (outbound; *right*) scenarios. CP: choice point. **c,d,** Three modes of organizing neuronal sequences in CA1 and PFC. **c,** Diagrammed are sharp-wave ripples (SWRs) occurring at the well, spatial fields (colored ovals) and theta oscillations during trajectory running. **d,** Illustrative ensembles from real data (simultaneously recorded cells in CA1 and PFC), showing replay sequences (~260 ms; brown shading), theta sequences (~100-200 ms; blue shadings), and spatial-field sequences at the behavioral timescale (~8 s). Each row represents a cell ordered and color-coded by field center on the C-to-L trajectory shown *top right*. Grey lines: actual position. Dashed vertical line: reward well exit. Black, brown, and dark blue lines: broadband, ripple-band (150-250 Hz), and theta-band (6-12 Hz) filtered LFPs from one CA1 tetrode, respectively.
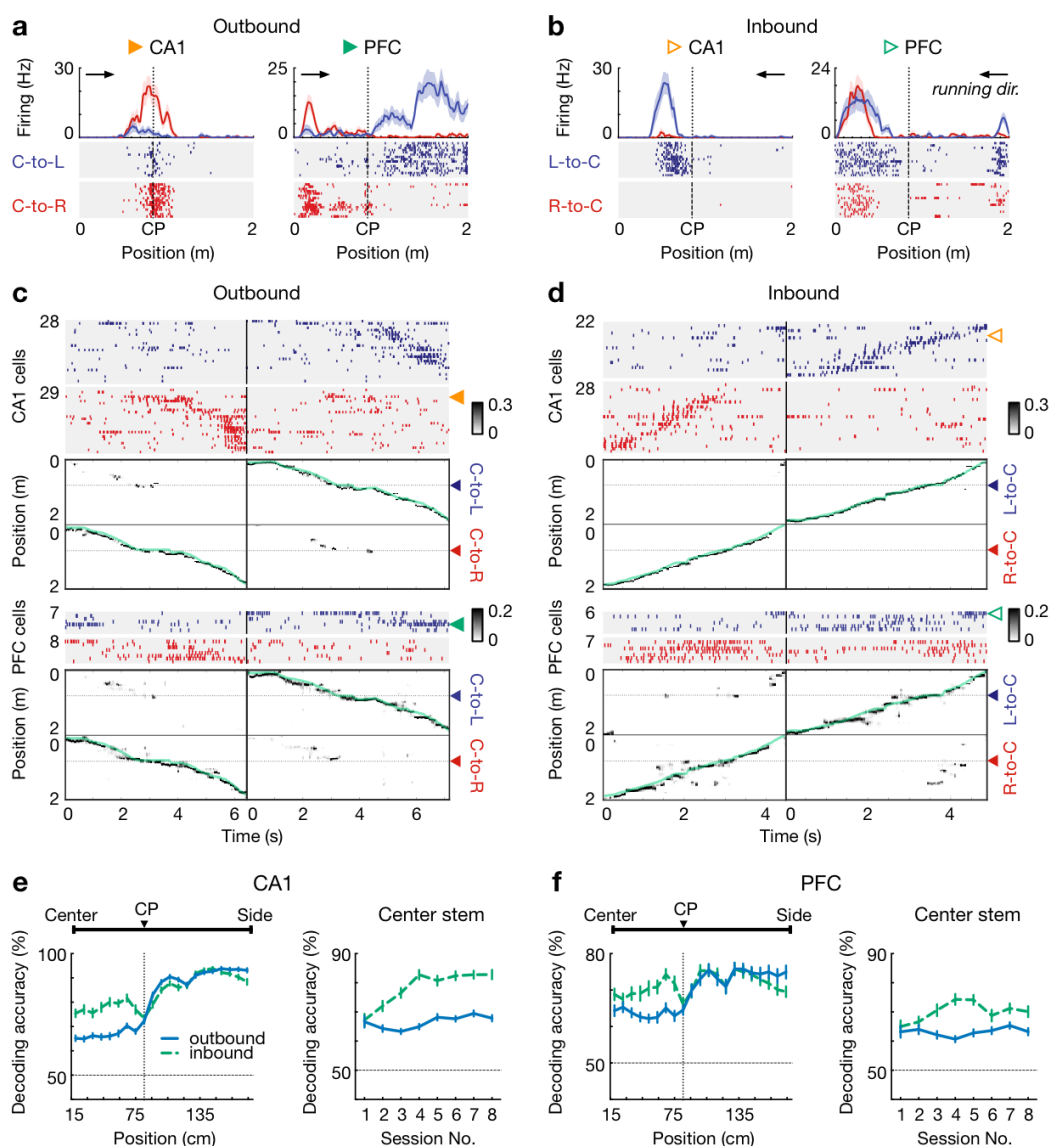
Fig. 2| Choice-predictive representations of behavioral-timescale sequences. a,b, Four trajectory-selective example cells during **(a)** outbound and **(b)** inbound navigation (shadings: SEMs; each row on the rasters represents a completed trajectory, or a trial; trajectory type denoted on the *left*; arrowheaded line indicates animal's running direction). **c,d,** Example choice-specific behavioral-timescale sequences. For each plot pair, the *top* illustrates a raster of trajectory-selective cell assemblies ordered by field centers on the preferred trajectory (L-selective assemblies in blue, R-selective assemblies in red); the *bottom* shows population decoding of animal's choice and locations at the behavioral timescale (bin = 120 ms; note that summed probability of each column across two trajectory types is 1). Green and yellow arrowheads indicate the example cells shown in **a,b**. Color bar: posterior probability. Green lines: actual position. Blue and red arrowheads: the CP. Note that the rasters only show trajectory-selective cells, whereas the population decoding was performed using all cells recorded in a given region. **e,f,** Behavioral-timescale sequences in **(e)** CA1 and **(f)** PFC predicted choices. *Left*: decoding accuracy of current choice over locations ($n = 9$ rats $\times$ 8 sessions); *Right*: decoding accuracy of current choice on the center stem across sessions. Note that the decoding performance is significantly better than chance (50%; all *p's* < 1e-4, rank-sum tests). Error bars: SEMs.
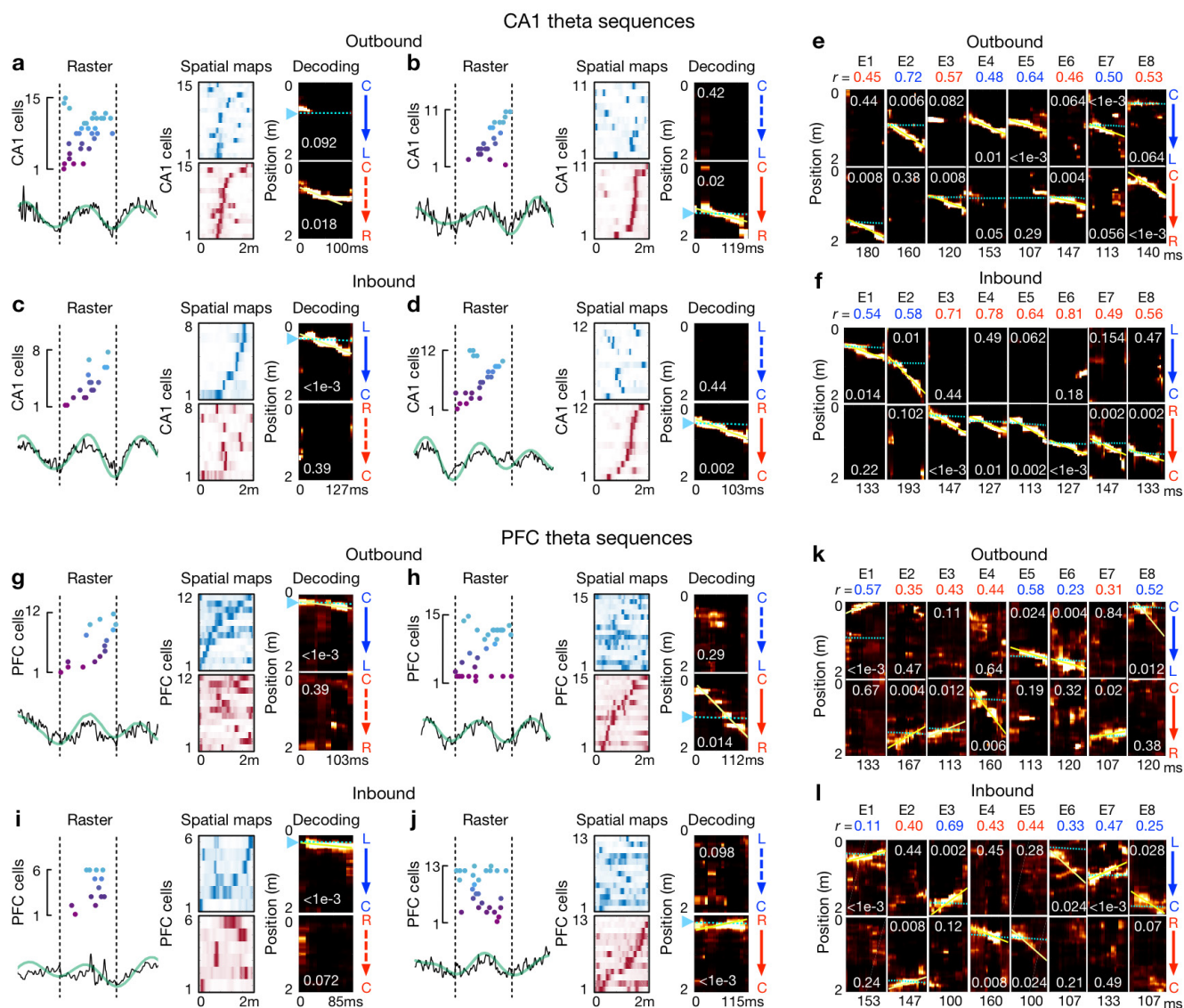
16

Fig. 3| Fast theta sequences in CA1 and PFC. a-d, Four examples of theta sequences in CA1 for **(a,b)** outbound and **(c,d)** inbound trajectories. *Left*: spikes ordered and color coded by field center on the decoded trajectory (see *Right*) over a theta cycle. Broadband (black) and theta-band filtered (green) LFPs from CA1 reference tetrode shown below. *Middle*: corresponding linearized spatial fields (blue colormap for L-side trajectory, red colormap for R-side trajectory). *Right*: Bayesian decoding with *p*-values based on shuffled data denoted (see **Methods**). Yellow lines: the best linear fit on the decoded trajectory. Cyan lines and arrowheads: actual position. Note that summed probability of each column across two trajectory types is 1. **e,f,** Example CA1 theta sequences across 8 sessions (or epochs, E1 to E8). Each column of plots represents a theta-sequence event. Sequence score (*r*) on the decoded trajectory denoted. **g-j,** Four examples of theta sequences in PFC for **(g,h)** outbound and **(i,j)** inbound trajectories. Data are presented as in **a-d**. **k,l,** Example PFC theta sequences across 8 sessions. Data are presented as in **e,f**.
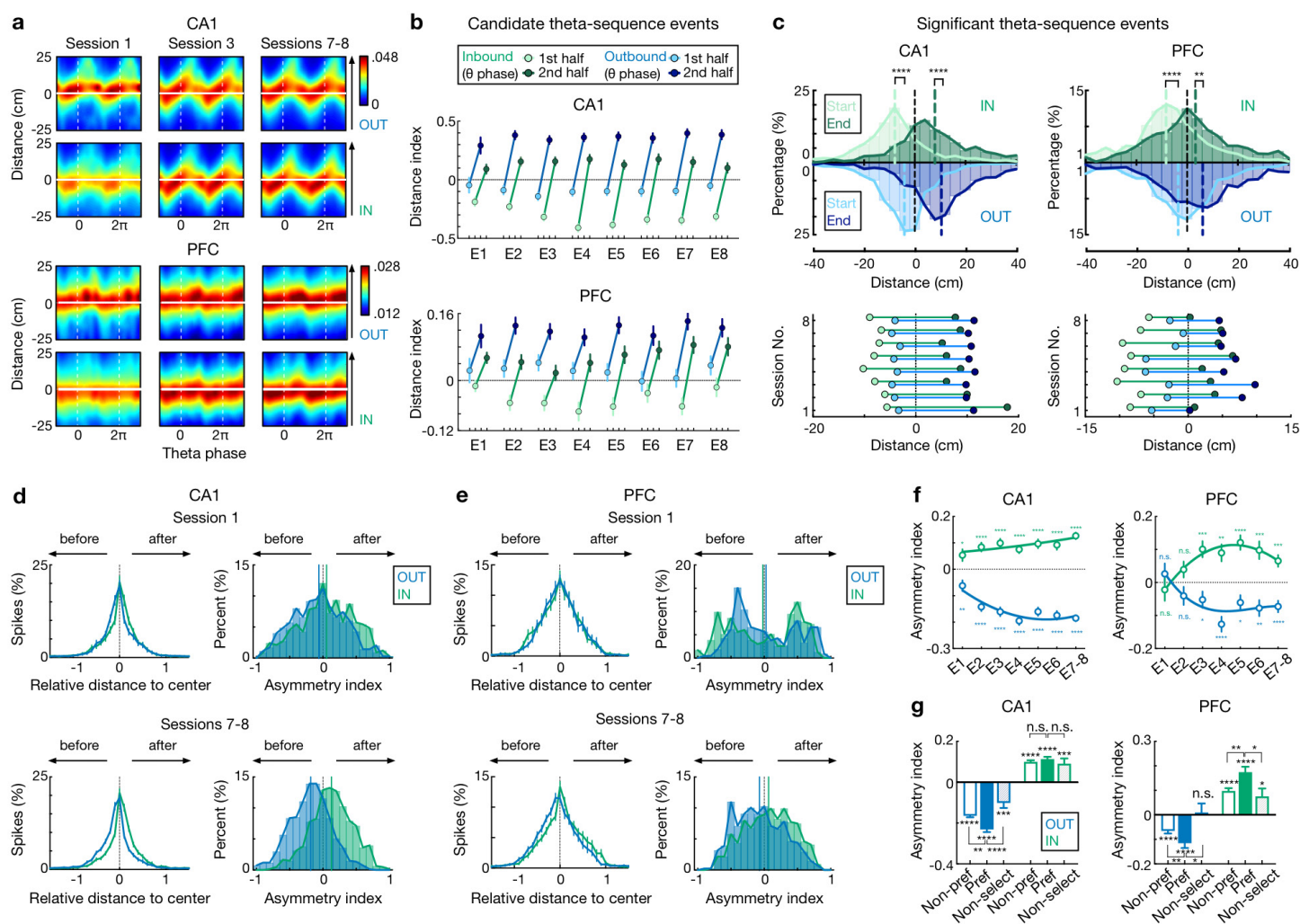
17

Fig. 4| Look-ahead of theta sequences during outbound versus inbound navigation. a, Theta sequences representing past, current, and future locations on outbound (OUT) and inbound (IN) trajectories in CA1 and PFC. Each plot shows the averaged Bayesian reconstruction of all forward candidate theta sequences (sequence score $r >$ 0), replicated over two theta cycles for visualization, relative to current position ($y = 0$; $y > 0$: ahead, or future location; $y < 0$: behind, or past location). Color bar: posterior probability. Arrowheaded line: animal's running direction. **b,** Distance index in CA1 (*top*) and PFC (*bottom*), compared the posterior probabilities on future versus past locations (< 0, biased to past; > 0, biased to future). 1st half of theta phases (light circles): $-\pi$ to 0; 2nd half of theta phases (dark circles): 0 to π. Error bars: 95% CIs. **c,** Distributions for start and end of reconstructed trajectories relative to actual position ($x = 0$) of all significant forward theta sequences. ****$p <$ 1e-4, **$p = 0.007$, Kolmogorov-Smirnov test. **d,e,** Spatial-field asymmetry during Session 1 (*top*) and Sessions 7-8 (*bottom*) in **(d)** CA1 and **(e)** PFC. Blue is for outbound fields (OUT) and green is for inbound fields (IN). *Left*: Averaged firing rate relative to spatial field center ($x = 0$) across all cells in the given sessions (error bars: SEMs). *Right*: Distributions of spatial-field asymmetry index (colored vertical lines: mean values). **f,** Spatial-field asymmetry across sessions (****$p <$ 1e-4, ***$p < 0.001$, **$p <$ 0.01, *$p < 0.05$, n.s. $p > 0.05$, signed-rank tests compared to 0). Lines are derived from polynomial fits. **g,** Trajectory-selective cells exhibit highly asymmetric fields on the preferred (Pref) trajectory compared to the non-preferred trajectory (Non-pref). Non-select: non-selective cells. *P*-values for each condition derived from signed-rank tests compared to 0; *p*-values across conditions derived from rank-sum tests (****$p <$ 1e-4, ***$p < 0.001$, **$p < 0.01$, *$p < 0.05$, n.s. $p > 0.05$). Data are presented as mean and SEMs.
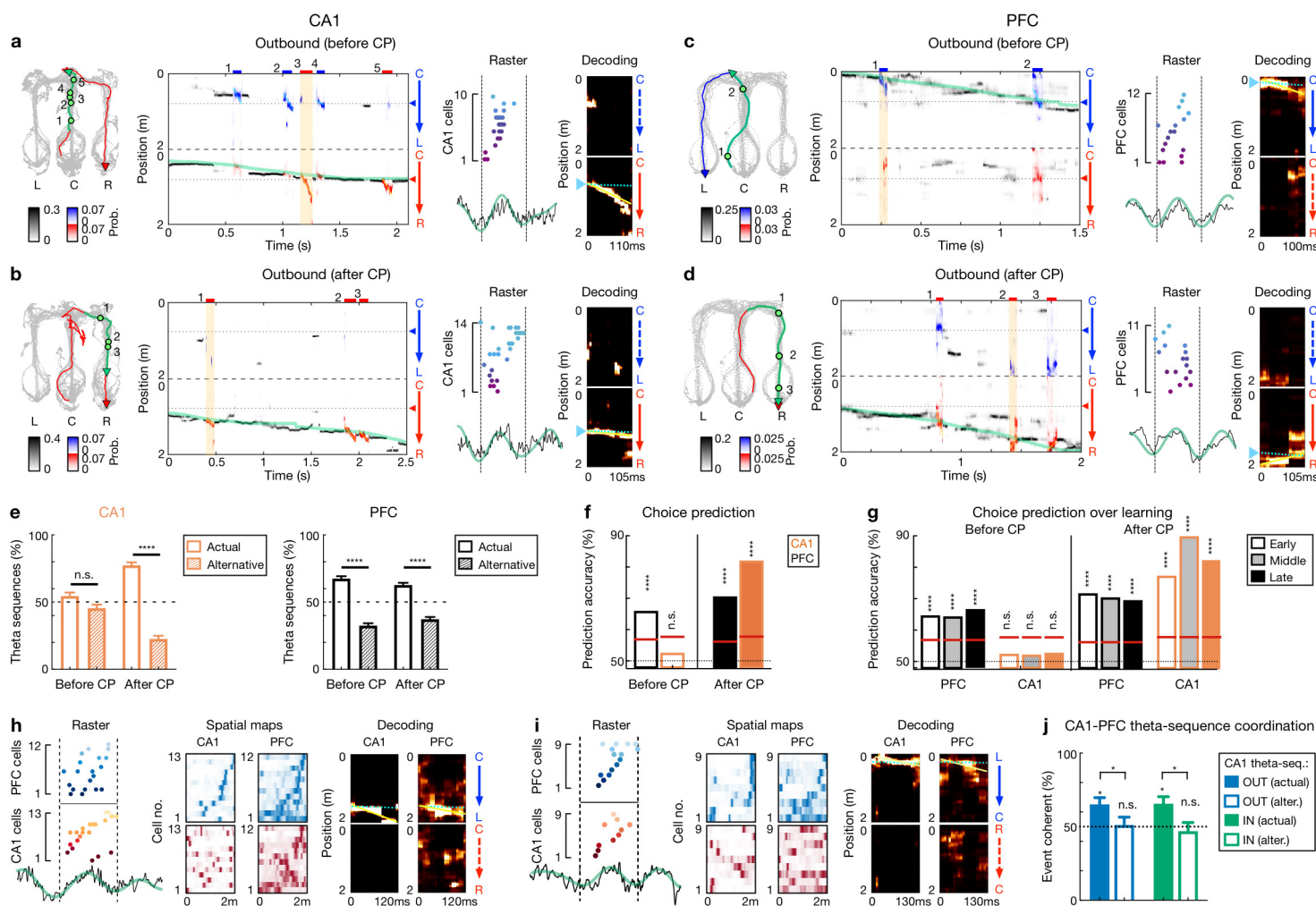
18

Fig. 5| Theta sequence representations of behavioral choices in CA1 and PFC. a-d, Four decoding examples during outbound navigation within the center stem (i.e., before CP) and after CP in **(a,b)** CA1 and **(c,d)** PFC. *Left*: Animal's behavior. Green line: the trajectory pass shown on the *middle*; Blue/red arrowheaded line: currently taken trajectory. Green circles: locations where theta-sequence events occurred (numbered corresponding to *middle*). *Middle*: Decoding plots. Data are presented as in **fig. 2c,d** (bin = 120 ms), except that whenever a theta sequence was detected, the decoding was performed on the theta timescale (bin = 30 ms) and color-coded by trajectory type for clarity (red or blue: R-side or L-side trajectory; bars above show decoded identity and timing of each event). Note that at both timescales, summed probability of each column across two trajectory types is 1. Yellow shading: example event with detailed view shown on the *right*. **e,** Percent of theta sequences representing actual or alternative choice before and after CP in CA1 (*left*) and PFC (*right*) (****$p < $1e-4, n.s. $p > 0.05$, session-by-session rank-sum paired tests). Error bars: SEMs. **f,** Trial-by-trial theta-sequence prediction of choice (****$p < 0.0001$, n.s., $p > 0.05$, trial-label permutation tests). Red horizontal lines: chance levels (i.e., 95% CIs of shuffled data) calculated by permutation tests. **g,** Theta-sequence prediction persists over sessions. Early: Sessions 1-3; Middle: Sessions 4-5; Late: Sessions 6-8. Data are presented as in **f**. Only correct trials are shown in **f,g**. **h-j** Coherent CA1-PFC theta sequences biased to actual choice. **h,j,** Two examples of coherent CA1-PFC theta sequences. **j,** Percent of coordinated CA1-PFC theta sequences coherently representing actual vs. alternative choices (for each condition from left to right: $p = 0.0312$, 0.94, 0.0312, 0.48, signed-rank test compared to 50%; for comparisons between two conditions from left to right, $p = 0.0312$ and 0.0469, rank-sum tests). OUT: outbound; IN: inbound. Alter.: alternative choice. Error bars: SEMs.
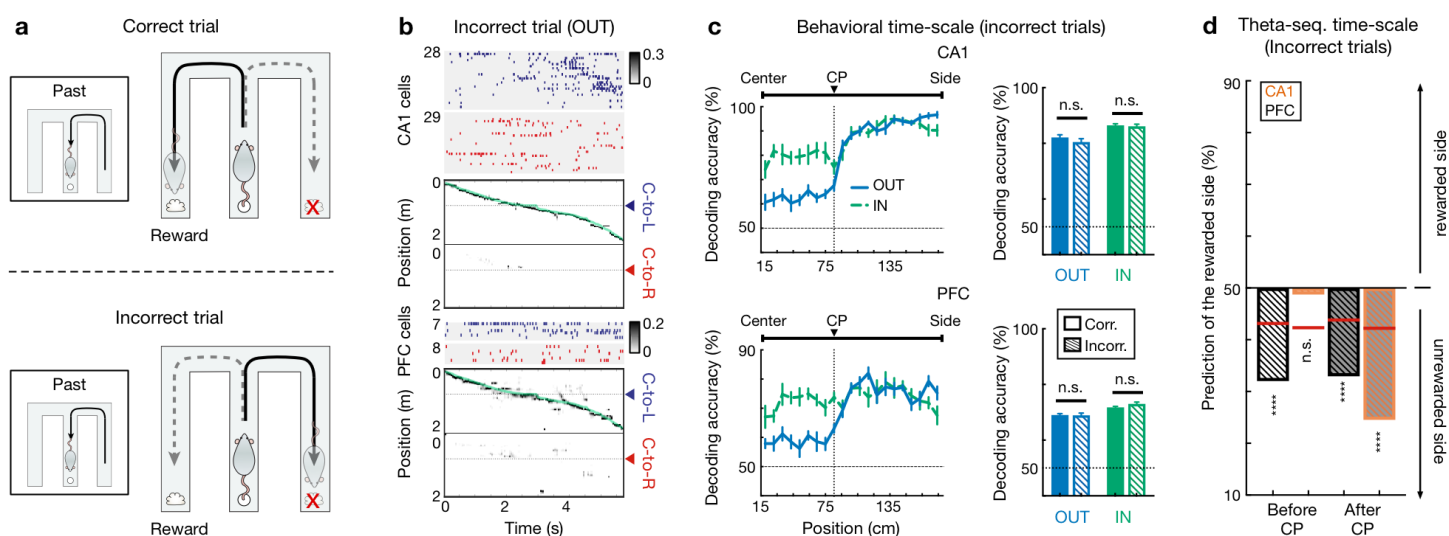
19

Fig. 6| Choice representations of behavioral-timescale and theta sequences were not impaired during incorrect trials. a, Illustration of a set of correct (*top*) and incorrect (*bottom*) trials. For incorrect trial, the actual choice is the unrewarded side. **b,c,** Choice representations of behavioral-timescale sequences were not impaired for incorrect trials. **b,** Rasters and population decoding during an incorrect outbound trial. Data are taken from the same session and animal and presented as in **Fig. 2c**. **c,** Choice decoding accuracy during incorrect trials is not significantly different from that during correct trials in CA1 (n.s., $p > 0.99$ for outbound, $= 0.67$ for inbound) and PFC (n.s., $p > 0.99$ for outbound, $= 0.11$ for inbound; Friedman tests with Dunn's *post hoc*). Corr.: correct trials; Incorr.: incorrect trials. Inbound trials for the incorrect condition were taken from the one right before an incorrect outbound trial (i.e., "Past" trial of the diagram shown in **a**). **d,** Choice representations of theta sequences were not impaired during incorrect trials (compare with **Fig. 5f**).
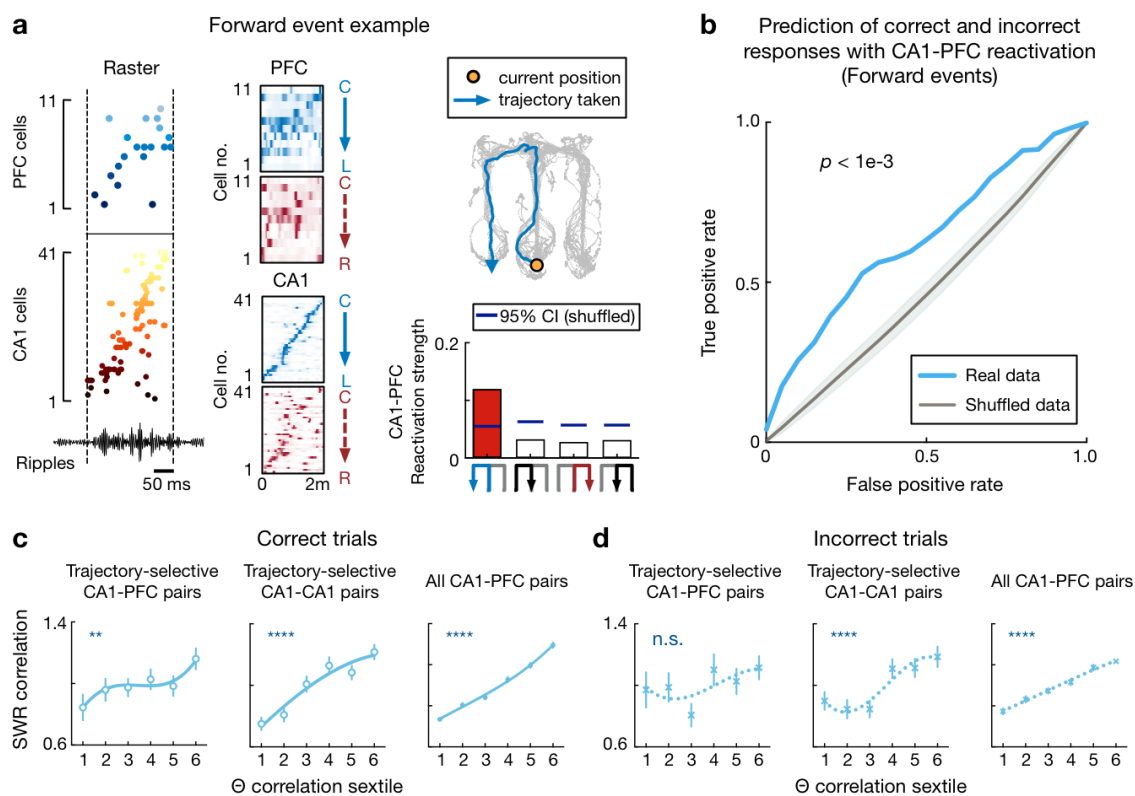
20

Fig. 7| Impairments in replay sequences prior to incorrect trials. a, Example forward CA1-PFC replay sequences representing actual future choice (see also **Fig. 1d** for this event with example cells, and ripples from a different tetrode). *Left:* Ordered raster plot during a SWR event (black line: ripple-band filtered LFPs from one CA1 tetrode). *Middle:* Corresponding spatial fields. *Top right:* Actual (immediate future) trajectory (orange circle: current position when replay sequences occurred). *Bottom right:* Reactivation strength (trajectory schematics on the *bottom*). Blue horizontal lines: 95% CIs computed from shuffled data. Red bar: the decoded trajectory. **b,** CA1-PFC replay strength predicts correct and incorrect responses. ROC curves were computed for the SVM classifiers (*p*-value from trial-label shuffling denoted; see **Methods**). Shadings: SDs. **c,d,** Specific impairment of reactivation of CA1-PFC trajectory-selective pairs during incorrect trials. **c,** Correct trials. **d,** Incorrect trials. For each panel, SWR correlation at the center well is plotted against peak theta correlation of cell pairs on the upcoming future trajectory (outbound), divided into six subgroups with equal number of cell pairs (sextiles). Symbols on the upper left corner indicate *p*-values (****: $p < 1e$-4, **: $p < 0.01$, n.s.: $p > 0.05$, Pearson correlation). Lines are derived from polynomial fits. Error bars: SEMs.

References

1.   Goldman-Rakic, P.S. Cellular basis of working memory. *Neuron* **14**, 477-485 (1995).

2.   Fuster, J. *The Prefrontal Cortex* (Academic Press, 2015).

3.   Sreenivasan, K.K. & D'Esposito, M. The what, where and how of delay activity. *Nat Rev Neurosci* **20**, 466-481 (2019).

4.   Miller, E.K., Lundqvist, M. & Bastos, A.M. Working Memory 2.0. *Neuron* **100**, 463-475 (2018).

5.   Fujisawa, S., Amarasingham, A., Harrison, M.T. & Buzsaki, G. Behavior-dependent short-term assembly dynamics in the medial prefrontal cortex. *Nat Neurosci* **11**, 823-833 (2008).

6.   Ito, H.T., Zhang, S.J., Witter, M.P., Moser, E.I. & Moser, M.B. A prefrontal-thalamo-hippocampal circuit for goal-directed spatial navigation. *Nature* **522**, 50-55 (2015).

7.   Pastalkova, E., Itskov, V., Amarasingham, A. & Buzsaki, G. Internally generated cell assembly sequences in the rat hippocampus. *Science* **321**, 1322-1327 (2008).

8.   Crowe, D.A., Averbeck, B.B. & Chafee, M.V. Rapid sequences of population activity patterns dynamically encode task-critical spatial information in parietal cortex. *J Neurosci* **30**, 11640-11653 (2010).

9.   Harvey, C.D., Coen, P. & Tank, D.W. Choice-specific sequences in parietal cortex during a virtual-navigation decision task. *Nature* **484**, 62-68 (2012).

10.   Bakhurin, K.I., Mac, V., Golshani, P. & Masmanidis, S.C. Temporal correlations among functionally specialized striatal neural ensembles in reward-conditioned mice. *J Neurophysiol* **115**, 1521-1532 (2016).

11.   Barnes, T.D., Kubota, Y., Hu, D., Jin, D.Z. & Graybiel, A.M. Activity of striatal neurons reflects dynamic encoding and recoding of procedural memories. *Nature* **437**, 1158-1161 (2005).

12.   Latimer, K.W., Yates, J.L., Meister, M.L., Huk, A.C. & Pillow, J.W. Single-trial spike trains in parietal cortex reveal discrete steps during decision-making. *Science* **349**, 184-187 (2015).

13.   Karlsson, M.P., Tervo, D.G. & Karpova, A.Y. Network resets in medial prefrontal cortex mark the onset of behavioral uncertainty. *Science* **338**, 135-139 (2012).

14.   Lundqvist, M.*, et al.* Gamma and Beta Bursts Underlie Working Memory. *Neuron* **90**, 152-164 (2016).

15.   Rich, E.L. & Wallis, J.D. Decoding subjective decisions from orbitofrontal cortex. *Nat Neurosci* **19**, 973-980 (2016).

16.   Johnson, A. & Redish, A.D. Neural ensembles in CA3 transiently encode paths forward of the animal at a decision point. *Journal of Neuroscience* **27**, 12176-12189 (2007).

17.   Papale, A.E., Zielinski, M.C., Frank, L.M., Jadhav, S.P. & Redish, A.D. Interplay between hippocampal sharp-wave-ripple events and vicarious trial and error behaviors in decision making. *Neuron* **92**, 975-982 (2016).

18.   Kay, K*., et al.* Constant Sub-second Cycling between Representations of Possible Futures in the Hippocampus. *Cell* **180**, 552-567 e525 (2020).

19.   Pezzulo, G., Donnarumma, F., Maisto, D. & Stoianov, I. Planning at decision time and in the background during spatial navigation. *Current opinion in behavioral sciences* **29**, 69-76 (2019).

20.   Shin, J.D., Tang, W. & Jadhav, S.P. Dynamics of Awake Hippocampal-Prefrontal Replay for Spatial Learning and Memory-Guided Decision Making. *Neuron* **104**, 1110-1125 e1117 (2019).

21.   Pfeiffer, B.E. & Foster, D.J. Hippocampal place-cell sequences depict future paths to remembered goals. *Nature* **497**, 74-79 (2013).

22.   Kaefer, K., Nardin, M., Blahna, K. & Csicsvari, J. Replay of Behavioral Sequences in the Medial Prefrontal Cortex during Rule Switching. *Neuron* **106**, 154-165 e156 (2020).

23.   Jadhav, S.P., Kemere, C., German, P.W. & Frank, L.M. Awake hippocampal sharp-wave ripples support spatial memory. *Science* **336**, 1454-1458 (2012).

24.   Fernandez-Ruiz, A*., et al.* Long-duration hippocampal sharp wave ripples improve memory. *Science* **364**, 1082-1086 (2019).

25.   Robbe, D. & Buzsaki, G. Alteration of theta timescale dynamics of hippocampal place cells by a cannabinoid is associated with memory impairment. *J Neurosci* **29**, 12597-12605 (2009).

26.   Petersen, P.C. & Buzsaki, G. Cooling of Medial Septum Reveals Theta Phase Lag Coordination of Hippocampal Cell Assemblies. *Neuron* **107**, 731-744 e733 (2020).

27.   Buzsaki, G., Peyrache, A. & Kubie, J. Emergence of Cognition from Action. *Cold Spring Harb Symp Quant Biol* **79**, 41-50 (2014).

28.   Kim, S.M. & Frank, L.M. Hippocampal lesions impair rapid learning of a continuous spatial alternation task. *PLoS One* **4**, e5494 (2009).

29.   Maharjan, D.M., Dai, Y.Y., Glantz, E.H. & Jadhav, S.P. Disruption of dorsal hippocampal - prefrontal interactions using chemogenetic inactivation impairs spatial learning. *Neurobiol Learn Mem* **155**, 351-360 (2018).

30.   Yu, J.Y. & Frank, L.M. Hippocampal-cortical interaction in decision making. *Neurobiol Learn Mem* **117**, 34-41 (2015).

31.   Wood, E.R., Dudchenko, P.A., Robitsek, R.J. & Eichenbaum, H. Hippocampal neurons encode information about different types of memory episodes occurring in the same location. *Neuron* **27**, 623-633 (2000).

32.   Frank, L.M., Brown, E.N. & Wilson, M. Trajectory encoding in the hippocampus and entorhinal cortex. *Neuron* **27**, 169-178 (2000).

33.   Wikenheiser, A.M. & Redish, A.D. Hippocampal theta sequences reflect current goals. *Nat. Neurosci.* **18**, 289-294 (2015).

34.   Skaggs, W.E., McNaughton, B.L., Wilson, M.A. & Barnes, C.A. Theta phase precession in hippocampal neuronal populations and the compression of temporal sequences. *Hippocampus.* **6**, 149-172 (1996).

35.   Siapas, A.G., Lubenov, E.V. & Wilson, M.A. Prefrontal phase locking to hippocampal theta oscillations. *Neuron* **46**, 141-151 (2005).

36.   Jadhav, S.P., Rothschild, G., Roumis, D.K. & Frank, L.M. Coordinated excitation and inhibition of prefrontal ensembles during awake hippocampal sharp-wave ripple events. *Neuron* **90**, 113-127 (2016).

37.   Gordon, J.A. Oscillations and hippocampal-prefrontal synchrony. *Curr Opin Neurobiol* **21**, 486-491 (2011).

38.   Hasz, B.M. & Redish, A.D. Spatial encoding in dorsomedial prefrontal cortex and hippocampus is related during deliberation. *Hippocampus* (2020).

39.   Zielinski, M.C., Shin, J.D. & Jadhav, S.P. Coherent Coding of Spatial Position Mediated by Theta Oscillations in the Hippocampus and Prefrontal Cortex. *J Neurosci* **39**, 4550-4565 (2019).

40.   Zheng, C., Bieri, K.W., Hsiao, Y.T. & Colgin, L.L. Spatial Sequence Coding Differs during Slow and Fast Gamma Rhythms in the Hippocampus. *Neuron* **89**, 398-408 (2016).

41.   Mehta, M.R., Quirk, M.C. & Wilson, M.A. Experience-dependent asymmetric shape of hippocampal receptive fields. *Neuron* **25**, 707-715 (2000).

42.   Shadlen, M.N. & Shohamy, D. Decision Making and Sequential Sampling from Memory. *Neuron* **90**, 927-939 (2016).

43.   Daw, N.D. & Dayan, P. The algorithmic anatomy of model-based evaluation. *Philos Trans R Soc Lond B Biol Sci* **369** (2014).

44.   Mattar, M.G. & Daw, N.D. Prioritized memory access explains planning and hippocampal replay. *Nat Neurosci* **21**, 1609-1617 (2018).

45.   Wang, M., Foster, D.J. & Pfeiffer, B.E. Alternating sequences of future and past behavior encoded within hippocampal theta oscillations. *Science* **370**, 247-250 (2020).

46.   Jezek, K., Henriksen, E.J., Treves, A., Moser, E.I. & Moser, M.B. Theta-paced flickering between place-cell maps in the hippocampus. *Nature* **478**, 246-249 (2011).

47.   Brandon, M.P., Bogaard, A.R., Schultheiss, N.W. & Hasselmo, M.E. Segregation of cortical head direction cell assemblies on alternating theta cycles. *Nat Neurosci* **16**, 739-748 (2013).

48.   Gupta, A.S., van der Meer, M.A., Touretzky, D.S. & Redish, A.D. Segmentation of spatial experience by hippocampal theta sequences. *Nat Neurosci* **15**, 1032-1039 (2012).

49.   Singer, A.C., Carr, M.F., Karlsson, M.P. & Frank, L.M. Hippocampal SWR activity predicts correct decisions during the initial learning of an alternation task. *Neuron* **77**, 1163-1173 (2013).

50.   Sadacca, B.F.*, et al.* The Behavioral Relevance of Cortical Neural Ensemble Responses Emerges Suddenly. *J Neurosci* **36**, 655-669 (2016).

51.   Tang, W., Shin, J.D., Frank, L.M. & Jadhav, S.P. Hippocampal-prefrontal reactivation during learning is stronger in awake compared with sleep states. *J Neurosci* **37**, 11789-11805 (2017).

52.   Smith, A.C.*, et al.* Dynamic analysis of learning in behavioral experiments. *J Neurosci* **24**, 447-461 (2004).

53.   Lubenov, E.V. & Siapas, A.G. Hippocampal theta oscillations are travelling waves. *Nature* **459**, 534-539 (2009).

54.   Schmidt, R.*, et al.* Single-trial phase precession in the hippocampus. *Journal of Neuroscience* **29**, 13232-13241 (2009).

55.   Kempter, R., Leibold, C., Buzsaki, G., Diba, K. & Schmidt, R. Quantifying circular-linear associations: hippocampal phase precession. *J Neurosci Methods* **207**, 113-124 (2012).

56.   Sanders, H.*, et al.* Temporal coding and rate remapping: Representation of nonspatial information in the hippocampus. *Hippocampus* **29**, 111-127 (2019).

57.   Souza, B.C. & Tort, A.B.L. Asymmetry of the temporal code for space by hippocampal place cells. *Sci Rep* **7**, 8507 (2017).

58.   Mizuseki, K., Sirota, A., Pastalkova, E. & Buzsaki, G. Theta oscillations provide temporal windows for local circuit computation in the entorhinal-hippocampal loop. *Neuron* **64**, 267-280 (2009).

59.   Deshmukh, S.S., Yoganarasimha, D., Voicu, H. & Knierim, J.J. Theta modulation in the medial and the lateral entorhinal cortices. *J Neurophysiol* **104**, 994-1006 (2010).

60.   Zhang, K., Ginzburg, I., McNaughton, B.L. & Sejnowski, T.J. Interpreting neuronal population activity by reconstruction: unified framework with application to hippocampal place cells. *J Neurophysiol* **79**, 1017-1044 (1998).

61.   Davidson, T.J., Kloosterman, F. & Wilson, M.A. Hippocampal replay of extended experience. *Neuron* **63**, 497-507 (2009).

62.   Feng, T., Silva, D. & Foster, D.J. Dissociation between the experience-dependent development of hippocampal theta sequences and single-trial phase precession. *J Neurosci* **35**, 4890-4902 (2015).

63.   Drieu, C., Todorova, R. & Zugaro, M. Nested sequences of hippocampal assemblies during behavior support subsequent sleep replay. *Science* **362**, 675-679 (2018).

64.   Farooq, U. & Dragoi, G. Emergence of preconfigured and plastic time-compressed sequences in early postnatal development. *Science* **363**, 168-173 (2019).

65.   Peyrache, A., Khamassi, M., Benchenane, K., Wiener, S.I. & Battaglia, F.P. Replay of rule-learning related neural patterns in the prefrontal cortex during sleep. *Nat Neurosci* **12**, 919-926 (2009).

66.   Chang, C.-C. & Lin, C.-J. Libsvm. *ACM Transactions on Intelligent Systems and Technology* **2**, 1-27 (2011).

67.   Gardner, R.J., Lu, L., Wernle, T., Moser, M.B. & Moser, E.I. Correlation structure of grid cells is preserved during sleep. *Nat Neurosci* **22**, 598-608 (2019).

68.   Trettel, S.G., Trimper, J.B., Hwaun, E., Fiete, I.R. & Colgin, L.L. Grid cell co-activity patterns during sleep reflect spatial overlap of grid fields during active behaviors. *Nat Neurosci* **22**, 609-617 (2019).

69.   Paxinos, G. & Watson, C. *The Rat Brain in Stereotaxic Coordinates* (Academic Press, 2004).

70.   Jones, M.W. & Wilson, M.A. Theta rhythms coordinate hippocampal-prefrontal interactions in a spatial memory task. *PLoS.Biol.* **3**, e402 (2005).

Methods

Subjects. Nine adult male Long-Evans rats (450-550 g, 4-6 months) were used in this study. All procedures were approved by the Institutional Animal Care and Use Committee at the Brandeis University and conformed to US National Institutes of Health guidelines. Data from six subjects have been reported in an earlier study[20].

Animal pre-training. Animals were habituated to daily handling for several weeks before training. After habituation, animals were food deprived to 85-90% of their *ad libitum* weight, and pre-trained to run on a linear track (~1-m long) for rewards (sweetened evaporated milk), and habituated to an high-walled, opaque sleep box (~30 × 30 cm) as described previously[23,36,51]. After the pre-training, animals were surgically implanted with a multi-tetrode drive.

Surgical implantation. Surgical implantation procedures were as previously described[20,23,36,51]. Eight animals were implanted with a multi-tetrode drive containing 30-32 independently moveable tetrodes targeting right dorsal hippocampal region CA1 (-3.6 mm AP and 2.2 mm ML) and right PFC (+3.0 mm AP and 0.7 mm ML). One animal was implanted with a multi-tetrode drive containing 64 independently moveable tetrodes targeting the bilateral CA1 of dorsal hippocampus (-3.6 mm AP and ±2.2 mm ML; **Supplementary Fig. 1a**, *left*) and PFC (+3.0 mm AP and ±0.7 mm ML; **Supplementary Fig. 1b**, *left*). On the days following surgery, hippocampal tetrodes were gradually advanced to the desired depths with characteristic EEG patterns (sharp wave polarity, theta modulation) and neural firing patterns as previously described[20,23,36,51]. One tetrode in corpus callosum served as hippocampal reference (CA1 REF), and another tetrode in overlying cortical regions with no spiking signal served as prefrontal reference (PFC REF). The reference tetrodes

27

reported voltage relative to a ground (GND) screw installed in skull overlying cerebellum. Electrodes were not moved at least 4 hours before and during the recording day. Following the conclusion of the experiments, micro-lesions were made through each electrode tip to mark recording locations (**Supplementary Fig. 1**).

Behavioral task. Following recovery from surgical implantation (~7-8 days), animals were food-deprived and again pre-trained on a linear track for at least two days before the W-track sessions started. During the recording day, animals were introduced to the novel W-track (**Fig. 1a**; ~80 × 80 cm with ~7-cm wide tracks) for the first time, and learned the task rules over 8 behavioral sessions (or epochs, denoted as E1-E8; **Supplementary Fig. 1c**). Each behavioral session lasted 15-20 mins and was interleaved with 20-30 min rest sessions in the sleep box (total recording duration $\cong$ 6 hours within a single day)[20]. On the W-maze, animals were rewarded for performing a hippocampus-[23,24,28] and prefrontal-dependent[29] continuous alternation task: returning to the center well after visits to either side well (left or right well; inbound trajectories), and choosing the opposite side well from the previously visited side well when starting from the center well (outbound trajectories). Rewards were automatically delivered in the reward wells (left well: L; right well: R; center well: C) triggered by crossing of an infrared beam by the animal's nose. Therefore, animals performed four types of trajectories during correct behavioral sequences in this task (**Fig. 1a**): center-to-left (C-to-L), left-to-center (L-to-C), center-to-right (C-to-R), and right-to-center (R-to-C). Among these trajectory types, C-to-L and C-to-R are outbound trajectories, while L-to-C and R-to-C are inbound trajectories. When animals were on the center stem, the two inbound trajectories thus represented possible past paths (one actual, and one alternative; **Fig. 1b**,

28

left), and the two outbound trajectories represented possible future paths (**Fig. 1b**, *right*). The learning curves were estimated using a state-space model (**Supplementary Fig. 1c**)[20,23,52].

Behavioral analysis. Locomotor periods, or theta states, were defined as periods with running speed > 5 cm/s, whereas immobility was defined as periods with speed ≤ 4 cm/s. The animal's arrival and departure at a reward well was detected by an infrared beam triggered at the well. The well entry was further refined as the first time point when the speed fell below 4 cm/s before the arrival trigger, whereas the well exit was defined as the first time point when the speed rose above 4 cm/s after the departure trigger[20]. The time spent at a reward well (i.e., immobility period at well) was defined as the period between well entry and exit. Only SWRs occurring during immobility periods at reward wells were analyzed in this study (see also *SWR detection*). The center stem of the W-maze was defined as the set of linear positions (see *Spatial fields and linearization*) between the center well and the center junction (i.e., choice point, CP). For a given behavioral trajectory, the before-CP period was defined as the time spent at the center stem, and the after-CP period was defined as the time spent at locations between 10 cm away from the center stem and the side well (**Fig. 5** and **Supplementary Fig. 5**). Therefore, for outbound trajectories, before-CP periods began when animals exited the center well and ended when animals reached the choice point (**Fig. 5**), and for inbound trajectories, before-CP periods began when animals entered the choice point from the side arm and ended when animals entered the center well (**Supplementary Fig. 5**).

Neural recordings. Data were collected using a SpikeGadgets data acquisition system (SpikeGadgets LLC)[20,51]. Spike data were sampled at 30 kHz and bandpass filtered between 600 Hz and 6 kHz. LFPs were sampled at 1.5 kHz and bandpass filtered between 0.5 Hz and 400 Hz.

The animal's position and running speed were recorded with an overhead color CCD camera (30 fps) and tracked by color LEDs affixed to the headstage. Single units were identified by manual clustering based on peak and trough amplitude, principal components, and spike width using custom software (MatClust, M. P. Karlsson) as previously described[20,36,51]. Only well isolated neurons with stable spiking waveforms were included[20].

Cell inclusion. Units included in analyses fired at least 100 spikes in a given session. Putative interneurons were identified and excluded based on spike width and firing rate criterion as previously described[23,36]. Peak rate for each unit was defined as the maximum rate across all spatial bins in the linearized spatial field (see *Spatial fields and linearization*). A peak rate ≥ 3 Hz was required for a cell to be considered as a place cell.

Spatial fields and linearization. Spatial fields were calculated only during locomotor periods (> 5 cm/s; all SWR times excluded) at positions with sufficient occupancy (> 20 ms). To construct the 1D linearized spatial fields on different trajectory types, animal's linear positions were first estimated by projecting its actual 2D positions onto pre-defined idealized paths along the track, and further classified as belonging to one of the four trajectory types[20,51]. The linearized spatial fields were then calculated using spike counts and occupancies in 2-cm bins of the linearized positions and smoothened with a Gaussian curve (4-cm SD). We found all linearized positions along each trajectory type were sufficiently covered by the spatial fields of CA1, as well as PFC, populations[20].

Trajectory selective index. To measure the trajectory selectivity of single cells, a trajectory selectivity index (*SI*) was calculated (**Supplementary Fig. 2g**) by comparing the mean firing rates on the Left- (or L-) versus Right- (or R-) side trajectories for outbound (C-to-L vs. C-to-R) and inbound (L-to-C vs. R-to-C), respectively:

$$SI = \frac{FR_L - FR_R}{FR_L + FR_R},$$

where FR_L is the mean firing rate on the L-side trajectory, and FR_R is for the R-side trajectory. Only cells that had at least one spatial field (peak firing rate $\geq$ 3 Hz) detected on either the L- or R-side trajectory were considered, and the spatial fields in different sessions were analyzed separately. A cell with $|SI| > 0.4$ in CA1, or $|SI| > 0.2$ in PFC was classified as trajectory-selective cells (**Supplementary Fig. 2g,h**)[18]. The trajectory type (L vs. R) with highest firing rate was designated as the cell's preferred (Pref) trajectory, and the other type designated as the non-preferred (Non-pref) trajectory.

SWR detection. Sharp-wave ripples (SWRs) were detected during immobility periods ($\leq$ 4 cm/s) as described previously[20,23,36,51]. In brief, LFPs from CA1 tetrodes relative to the CA1 reference tetrode were filtered into the ripple band (150-250 Hz), and the envelope of the ripple-filtered LFPs was determined using a Hilbert transform. SWRs were initially detected as contiguous periods when the envelope stayed above 3 SD of the mean on at least one tetrode, and further refined as times around the initially detected events during which the envelope exceeded the mean. For replay and reactivation analysis, only SWRs with a duration $\geq$ 50 ms were included as in previous studies[20,21].

31

Theta phases and theta cycles. Peaks and troughs of theta oscillations, as well as theta phases, were identified on the band-passed (6-12 Hz) LFPs from the CA1 reference tetrode[36,53]. To precisely define a theta cycle for theta sequence detection, theta phase locking of each cell in CA1 was calculated across locomotor periods (> 5 cm/s) in each session using the methods developed in previous reports[35,36]. A phase histogram was then calculated by averaging across all phase-locked CA1 cells (Rayleigh tests at $p < 0.05$) in each session, and the phase with minimum cell firing was used to separate theta cycles in the given session (approximately valley-to-valley of hippocampal REF theta, or peak-to-peak of hippocampal fissure theta)[48].

Theta phase precession. Theta phase precession was examined in linearized spatial fields with a peak rate ≥ 3 Hz, and multiple fields of a single cell were analyzed separately (e.g., **Supplementary Fig. 4a**, *top right*). For each firing peak of linearized spatial fields detected (using MATLAB *findpeaks* function with a 20-cm minimal peak distance), a spatial field was defined as contiguous positions with rate > 10% of the peak rate, and at least 8 cm large (**Supplementary Fig. 4a,b**)[54]. For spikes within each spatial field, phase precession was computed using a circular-linear fit as previously described (*cl_corr* function in the *measure_phaseprec* toolbox; https://github.com/HoniSanders/measure_phaseprec)[55,56]. The slope, correlation coefficient (r), and its p-value from the circular-linear regression were reported (**Supplementary Fig. 4**).

Theta power and coherence. Power spectra and coherograms were computed from the LFPs referenced to GND using multitaper estimation methods from the Chronux toolbox (http://chronux.org; version 2.12)[20]. We obtained the SD and mean for each frequency across a given session, and normalized the power of that frequency as a z-score (**Supplementary Fig. 7b**).

32

Coherence between a pair of CA1 and PFC tetrodes was calculated during locomotor periods (> 5 cm/s; locations within 15 cm of the reward well were excluded to prevent contamination from SWR activity). Coherograms averaged over all available CA1-PFC tetrode pairs with simultaneously recorded LFPs were shown in **Supplementary Fig. 7c,d**. Theta power and coherence were measured as the mean power and coherence between 6-12 Hz, respectively.

Spatial field asymmetry. For cells showing significant phase precession (circular-linear regression at $p < 0.05$), we further analyzed their spatial field asymmetry (**Fig. 4d-g**). Only fields with the highest peak rate of a single cell for each trajectory type, and at least 20 cm large, were used. The spatial fields were then binned into 10% field length relative to field center[57], and the asymmetry index (*AI*) was calculated as:

$$AI = \frac{A_R - A_L}{A_R + A_L},$$

where A_R denoted the area under the firing rate profile to the right of the field center (i.e., $x > 0$ in **Fig. 4d,e**), while A_L represented the same to the left of the field center (i.e., $x < 0$ in **Fig. 4d,e**). Therefore, a negative *AI* corresponds to a spatial field with an extended initial tail.

Theta cycle skipping. To quantify theta cycle skipping in single cells (**Supplementary Fig. 6**), we measured a cycle skipping index (CSI) on their auto-correlograms (ACGs). Data on different trajectory types were analyzed separately, and thus a single cell could contribute to more than one ACG. For each ACG, data was restricted to locomotor periods (> 5 cm/s) that lasted at least 1.5 s, and with at least total 100 spikes[18]. Each ACG was first estimated as a histogram of nonzero lags across the interval ± 400 ms (bin = 10 ms)[18,47], and was further corrected for the triangular shape caused by finite duration data[18,58]. The corrected ACG was then smoothed (Gaussian kernel, SD =

20 ms) and peak-normalized. To detect the theta-modulated peaks of ACGs, power spectra for ACGs were generated using FFT, and the relative theta power of an ACG was calculated by dividing its power in the theta band (6-10 Hz) by its total power in the 1-50 Hz range[59]. An ACG with relative theta power > 0.15 was considered theta-modulated. For all theta-modulated ACGs, the ACGs were band-pass filtered between 1 and 10 Hz[59], and the amplitudes of the first and second theta peaks on the filtered ACG were then determined by finding a first peak (p_1) near $t =$ 0 in the 90-200 ms window, and the second peak (p_2) near $t = 0$ in the 200-400 ms window, as described previously[18]. The CSI was then determined as:

$$CSI = \frac{p_2 - p_1}{\max(p_1, p_2)},$$

The CSI ranges between −1 and 1, and higher values indicate more theta cycle skipping.

Sequence analysis. Sequence analysis here focused on three different ensemble sequences: behavioral-timescale sequences, theta sequences, and replay sequences (**Fig. 1c,d**). To evaluate neural representations at the ensemble level, Bayesian decoding was implemented as previously described[20,51,60,61]: a memoryless Bayesian decoder was built for different trajectory types (for outbound, C-to-L vs. C-to-R; for inbound, L-to-C vs. R-to-C) to estimate the probability of animals' position given the observed spikes (Bayesian reconstruction; or posterior probability matrix):

$$P(X, Tr | \mathbf{spikes}) = \frac{P(\mathbf{spikes} | X, Tr) P(X, Tr)}{P(\mathbf{spikes})},$$

where X is the set of all linear positions on the track for different trajectory types (i.e., Tr; Tr $\in \{L, R\}$, where L represents the L-side trajectory, R represents the R-side trajectory), and we

34

assumed a uniform prior probability over X and Tr. Assuming that all N cells active in a sequence fired independently and followed a Poisson process:

$$P(\mathbf{spikes}|X,Tr) = \prod_{i=1}^{N} P(spikes_i|X,Tr) = \prod_{i=1}^{N} \frac{\left(\tau f_i(X,Tr)\right)^{spikes_i} e^{-\tau f_i(X,Tr)}}{spikes_i!},$$

where τ is the duration of the time window (see below), $f_i(X,Tr)$ is the expected firing rate of the i-th cell as a function of sampled location X and trajectory type Tr, and $spikes_i$ is the number of spikes of the i-th cell in a given time window. Therefore, the posterior probability matrix can be derived as follows:

$$P(X,Tr|\mathbf{spikes}) = C\left(\prod_{i=1}^{N} f_i(X,Tr)^{spikes_i}\right) e^{-\tau \sum_{i=1}^{N} f_i(X,Tr)},$$

where C is a normalization constant such that $\sum_{k=1}^{2}\sum_{j=1}^{D} P(x_j,tr_k|\mathbf{spikes}) = 1$ (x_j is the j-th position bin, D is the total length of the track, and tr_k is the k-th trajectory type; $k = 1$ or 2, representing L- or R-side trajectory, respectively).

Specifically, for behavioral-timescale sequences, the Bayesian decoder was used to decode animal's current location (x) and choice (tr) (**Fig. 2** and **Supplementary Fig. 2**) as in previous studies[20]. Data was restricted to locomotor periods (> 5 cm/s; locations within 15 cm of the reward well were excluded for decoding to prevent contamination from SWR activity), and binned into 120-ms bins (i.e., $\tau = 120$ ms; moving window with 60 ms overlap). For each time bin, the location and choice (i.e., trajectory type) with maximum decoded probability was compared to the actual position and choice of the animal in that bin (**Fig. 2c-f** and **Supplementary Fig. 2a-f**). Decoding error of positions in this bin was determined as the linear distance between estimated position and actual position (**Supplementary Fig. 2e,f**), and the accuracy of animal's choices decoded was reported (**Fig. 2e,f**).

35

For theta sequences, we first defined candidate events as theta cycles with at least 5 cells active in a given brain region (CA1 or PFC). Only theta cycles with running speed > 10 cm/s, and a duration ranging from 100 to 200 ms were used[62]. A time window of 20 ms (i.e., $\tau = 20$ ms; moving window with 10 ms overlap) was used to examine theta sequence structure at a fast, compressed timescale. To identify sequential structure within a theta cycle, two measures were adapted from previous theta-sequence studies[40,62-64]. In the first method, a weighted correlation[62,64], $r(x,t|\mathbf{Pmat})$, was calculated for the posterior probability matrix of each trajectory type ($\mathbf{Pmat}$, $D \times T$, D is the total number of spatial bins, and T is the total number of temporal bins). The weighted means were computed across locations (x) and time (t) as:

$$E_X(x|\mathbf{Pmat}) = \frac{\sum_{i=1}^{T}\sum_{j=1}^{D} Pmat_{ij}x_j}{\sum_{i=1}^{T}\sum_{j=1}^{D} Pmat_{ij}},$$

$$E_T(t|\mathbf{Pmat}) = \frac{\sum_{j=1}^{D}\sum_{i=1}^{T} Pmat_{ij}t_i}{\sum_{j=1}^{D}\sum_{i=1}^{T} Pmat_{ij}},$$

and the weighted covariance, $covar(x,t|\mathbf{Pmat})$, was computed as:

$$covar(x,t|\mathbf{Pmat}) = \frac{\sum_{i=1}^{T}\sum_{j=1}^{D} Pmat_{ij}\left(x_j - E_X(x|\mathbf{Pmat})\right)\left(t_i - E_T(t|\mathbf{Pmat})\right)}{\sum_{i=1}^{T}\sum_{j=1}^{D} Pmat_{ij}},$$

where t_i is the i-th temporal bin, and x_j is the j-th spatial bin of the posterior probability matrix ($\mathbf{Pmat}$). The weighted correlation was then calculated as:

$$r(x,t|\mathbf{Pmat}) = \frac{covar(x,t|\mathbf{Pmat})}{\sqrt{covar(t,t|\mathbf{Pmat})covar(x,x|\mathbf{Pmat})}},$$

and the weighted correlation was reported as the sequence score (r).

In the second method, we measured whether the decoded positions in successive temporal bins of the posterior probability matrix were tightly arranged along an oblique line as previously reported[61-63]. Briefly, the best-fit line of a theta sequence (e.g., yellow lines in **Fig. 3**) was determined by a fitted line that yielded maximum posterior probability in an 8-cm vicinity (d). For a given candidate line with a slope v and an intercept ρ, the average likelihood R that the decoded position is located within a distance d of that line is:

$$R(v,\rho) = \frac{1}{n}\sum_{k=0}^{n-1} P\big(|pos - vk \cdot \Delta t| \leq d\big),$$

where k is the temporal bin of the posterior probability matrix, and Δt is the moving step of the decoding window (i.e., 10 ms). To determine the best-fit line for each theta sequence, we densely sampled the parameter space of v and ρ ($v > 1$ m/s to exclude stationary events) to find the value that maximized R (R_{max}, i.e., goodness-of-fit).

In order to assess the significance of theta sequences, we circularly shifted the space-bins of the posterior probability matrix ($n = 1000$ times) as described previously[40,63,64], and calculated the weighted correlation and the goodness-of-fit from the shuffled data. A sequence was considered significant if it met two criteria: first, its sequence score (i.e., weighted correlation) exceeded the 97.5th percentile or was below the 2.5th percentile (for reverse sequences) of the shuffled distributions; and its goodness-of-fit (R_{max}) was higher than the 95th percentile of their shuffles. We considered the significant trajectory type as the decoded trajectory, and if more than one trajectory type were significant, the trajectory with the highest sequence score was considered as the decoded trajectory. For plotting purposes only, a moving window (30 ms, advanced in steps of 5 ms) was used for displaying theta sequences (**Figs. 3** and **5** and **Supplementary Fig. 5**).

The detection of replay sequences has been described previously[20]. Briefly, candidate replay events were defined as the SWR events during which ≥ 5 place cells fired. Each candidate event

was then divided into 10-ms non-overlapping bins (i.e., τ = 10 ms), and decoded based on the Bayes' rule described above. The assessment of significance for replay events was implemented by a Monte Carlo shuffle, in which the R-squared from linear regression on the temporal bins versus the locations of the posterior probability matrix was compared to the R-squared derived from the shuffled data (i.e., time shuffle, circularly shuffling temporal bins of the posterior probability matrix). A candidate event with an R-squared that exceeded the 95th percentile of their shuffles (i.e., $p < 0.05$) was considered as a replay event.

For SWR events with significant CA1 replay sequences detected, we further measured CA1-PFC reactivation during these events (**Fig. 7** and **Supplementary Fig. 9**) as described previously[20]. We only analyzed the events where $\geq$ 5 place cells and $\geq$ 5 PFC cells fired. Briefly, for an event with N CA1 and M PFC cells active, a ($N \times M$) synchronization matrix during RUN ($\mathbf{C_{RUN}}$) was calculated with each element ($C_{i,j}$) representing the Pearson correlation coefficient of the linearized spatial fields on a certain trajectory type (see *Spatial fields and linearization*) of the i-th CA1 cell and the j-th PFC cell. To measure the population synchronization pattern during the SWR, the spike trains during the SWR were divided into 10-ms bins and z transformed[20,65]. The ($N \times M$) synchronization matrix during the SWR ($\mathbf{C_{SWR}}$) was then calculated with each element ($C_{i,j}$) representing the correlation of the spike trains of a CA1-PFC cell pair. Finally, the reactivation strength of this event for each trajectory type was measured as the correlation coefficient (R) between the population matrices, $\mathbf{C_{RUN}}$ and $\mathbf{C_{SWR}}$.

Theta-sequence predication of behavioral choices. For theta-sequence prediction of behavioral choices (**Figs. 5f,g** and **6d** and **Supplementary Fig. 5**), trial-by-trial classification analysis was performed using support vector machines (SVMs) through the *libsvm* library (version 3.12)[66]. For

each region (CA1 or PFC), two independent SVMs were trained for before-CP and after-CP periods. For each trial, the numbers of theta sequences representing the actual versus the alternative choice during a given period (before CP, or after CP) were used as a feature ($n = 2$) to predict the current choice ($k = 2$, L or R). All classifiers were C-SVMs with a radial basis function (Gaussian) kernel and trained on correct trials. Hyperparameter (C and γ; regularization weight and radial basis function width, respectively) selection was performed using a random search method with leave-one-out cross-validation to prevent overfitting. The selected hyperparameters were then used to report the leave-one-out cross-validation accuracy. The percentage of correctly inferred trials was computed across all training/test trial combinations to give prediction accuracy. The significance of this prediction was determined by comparing to the distribution of shuffled data by randomly shuffling the trial labels (L or R), and this shuffled dataset was used to train a classifier in the same way as the actual dataset. A prediction accuracy based on the actual dataset that was higher than the 95th percentile of its shuffles ($p < 0.05$) was considered as significant. Only trials with at least one theta sequence for actual and alternative choices were used for prediction.

CA1-PFC reactivation predication of correct and incorrect responses. For prediction of correct and incorrect responses with CA1-PFC reactivation (**Fig. 7b** and **Supplementary Fig. 9c**), SVMs were used similar to the theta-sequence prediction analysis (see above). Two independent SVMs were trained on forward and reverse replay events. For each trial, the averaged CA1-PFC reactivation strength for the actual versus the alternative trajectory across all reactivation events during immobility at the reward well *prior* to the trial was used as a feature ($n = 2$; **Supplementary Fig. 9a**) to predict correct versus incorrect responses ($k = 2$, correct or incorrect, regardless of which side arm that the animals choose[49]). The significance of this prediction was determined by

comparing it to the distribution of shuffled data by randomly shuffling the trial labels (correct or incorrect), and this shuffled dataset was used to train a classifier in the same way as the actual dataset. Given the unbalanced nature of the dataset (a lot more correct trials than incorrect trials), we resampled the incorrect trials (with replacement) to match the correct trials, and used ROC analysis to measure the predictive power of the classifiers. The area under each ROC curve (AUC) was computed[33], and an AUC based on the actual dataset that was higher than the 95th percentile of its shuffles ($p < 0.05$) was considered as significant. Only trials with at least one reactivation event of the given type (forward or reverse) were used for prediction.

CA1-PFC pairwise correlation. Spike-time pairwise correlation during theta and SWR states were calculated as previously described[23,35,36,51] (**Fig. 7c,d** and **Supplementary Fig. 9d,e**). In brief, cross-correlation was computed using 10 ms bins, normalized by the mean firing rates of the neurons, and followed by smoothing (Gaussian kernel, SD = 30 ms). The peak of the cross-correlations was determined in a ±200 ms window around the 0-ms lag. Given the different firing rates on different trajectory types, correlations of all cell pairs for a given trajectory type were scaled by their average value for that trajectory (i.e., transformed correlation)[67,68]. For trajectory-selective cell pairs in **Fig. 7c,d** and **Supplementary Fig. 9d,e**, cells with the same trajectory preference were paired to calculate the cross-correlation.

Statistical Analysis. Data analysis was performed using custom routines in MATLAB (MathWorks) and GraphPad Prism 8 (GraphPad Software). We used nonparametric and two-tailed tests for statistical comparisons throughout the paper, unless otherwise noted. We used Kruskal-Wallis or Friedman test for multiple comparisons, with *post hoc* analysis performed using a Dunn's

test. $P < 0.05$ was considered the cutoff for statistical significance. Unless otherwise noted, values and error bars in the text denote means $\pm$ SEMs. No statistical methods were used to pre-determine sample sizes, but our sample sizes are similar to those generally employed in the field.

Data and code availability: The reported data and code used are archived on file servers at Brandeis University, and are available from the corresponding author upon request.

Author contributions: W.T., J.D.S. and S.P.J. designed the study. S.P.J. proposed and directed the project. J.D.S carried out the experiments and collected the data. W.T. analyzed the results and prepared the figures. W.T., J.D.S. and S.P.J. wrote the paper.

Competing interests: Authors declare no conflicts of interest.

Correspondence and requests for materials should be addressed to S.P.J.